Seismic radiation from dynamic coalescence, and the reconstruction of dynamic source parameters on a planar fault

Nobuki Kame and Koji Uchida*

Department of Earth and Planetary Sciences, Faculty of Sciences, Kyushu University, Hakozaki 6-10-1, Higashi-ku, Fukuoka 812-8581, Japan.
E-mail: kame@geo.kyushu-u.ac.jp

SUMMARY

The dynamic coalescence of two mode II cracks on a planar fault is simulated here using the elastodynamic boundary integral equation method. We focus on the complexity of the resultant slip rate and seismic radiation in the crack coalescence model (CCM) and on the reconstruction of a single crack model (SCM) that can reproduce the CCM waveforms from heterogeneous source parameters rather than coalescence. Simulation results reveal that localized higher slip rates are generated by coalescence as a result of stress interaction between the approaching crack tips. The synthesized seismic radiation exhibits a distinct coalescence phase that has striking similarities to stopping phases in the radiation and propagation properties. The corresponding SCM yields a singular increase in the stress drop distribution, which is accompanied by a sudden decrease in it across the point of coalescence in the CCM. This implies that the generation of high-frequency radiation is more efficient from coalescence than from stopping, although both phenomena exhibit the same strong ω^{-2}-type displacement spectra.

Key words: Numerical solutions; Earthquake dynamics; Earthquake ground motions; Dynamics and mechanics of faulting; Mechanics, theory, and modelling.

1 INTRODUCTION

Numerous recent inversions of strong motion data have revealed very complex slip functions and heterogeneous distributions of dynamic source parameters such as stress drop, strength excess and critical slip-weakening distance (e.g. Quin 1990; Ide & Takeo 1997). In such inversions, it has typically been assumed that a monotonically spreading rupture front is generated from a flat fault model. These assumptions are required largely because waveform data have insufficient resolution to determine the precise geometry of either the rupture fronts or the fault structures.

On the other hand, substantial progress has also been made in the numerical analysis of spontaneous rupture propagation. In the first phase of this research, the effects of heterogeneous source parameters on the dynamic rupture process have been investigated for flat source models. Important physical concepts, such as very high-strength 'barriers' and large stress drop 'asperities', have emerged from the early studies (e.g. Das & Aki 1977; Kostrov & Das 1988). More recently, advanced numerical methods have enabled us to simulate more realistic processes such as rupture front interaction (Yamashita & Umeda 1994; Kame & Yamashita 1997; Fukuyama & Madariaga 2000) and rupture propagation on geometrically complex faults (Harris & Day 1993; Kame & Yamashita 1999a; Aochi

& Fukuyama 2002; Ando *et al.* 2007; Kame *et al.* 2008). It has been demonstrated that both processes exert significant effects on the complexity of the slip rate and rupture propagation (Chatterjee & Knopoff 1990; Umeda *et al.* 1996; Kame & Yamashita 1999b, 2003; Dunham *et al.* 2003; Kame *et al.* 2003; Bhat *et al.* 2004).

It is important to consider what heterogeneous source parameters will be inferred from an inversion analysis if the assumptions, on which it is based, do not fully pertain to the actual earthquake being studied. To address this topic, we consider here a rupture process, in which rupture fronts interact and finally coalesce on a flat fault. Obviously, this scenario does not meet one of the major inversion assumptions of a 'monotonically spreading rupture front'. We then consider another event that produces the same seismic radiation due, solely, to stress and strength heterogeneities on the fault and not to any coalescence. Because the assumption of a 'monotonically spreading rupture front' is totally satisfied in this case, the heterogeneity can be regarded as the 'apparent' heterogeneity corresponding to unmodelled rupture coalescence, which could have been inferred from a conventional inversion analysis. Investigating such apparent heterogeneity is one of main goals of the work presented here.

Another point of interest here is the seismic radiation generated by dynamic coalescence. The generation of localized higher slip rates due to coalescence has been reported in many rupture front interaction simulations, (Yamashita & Umeda 1994; Fukuyama & Madariaga 2000; Dunham *et al.* 2003) and its significant effect on high-frequency radiation has been anticipated. However, the

*Now at: Nihon Unisys Ltd., Japan.

resultant seismic waveforms have been synthesized only at particular stations and the overall radiation and propagation characteristics remain unclear. As to the non-planar fault dynamics, Adda-Bedia & Madariaga (2008) and Madariaga *et al.* (2006) have recently calculated the seismic radiation emanating from a kink on a 2-D fault and found a distinct cylindrical phase, enriched with high-frequency radiation that is emitted from the kink. Accordingly, it is also useful to consider in detail here the seismic radiation accompanying dynamic coalescence and to investigate its characteristics.

To address these issues, we employ a crack coalescence model (CCM) consisting of two mode II cracks on a planar fault. We simulate the dynamic coalescence process in the CCM for homogeneous source parameters and investigate the resulting complexity of the slip rate. We then synthesize the seismic radiation of the CCM and determine the characteristics of a coalescence phase. We next attempt to reconstruct a seismically comparable single crack model (SCM), using heterogeneous source parameters. In this context, 'seismically comparable' means that it yields similar seismic waveforms to the CCM such as the coalescence phase generated from heterogeneity within a SCM. Based on the specific coalescence heterogeneity inferred, we finally discuss the mechanism of high-frequency radiation from dynamic coalescence.

2 MODEL AND METHOD

2.1 Crack coalescence model (CCM)

Earthquake faulting is modelled here in terms of the dynamic growth of mode II cracks in an unbounded homogeneous isotropic elastic medium. We use Cartesian coordinates (x, y) and align the fault plane with the x-axis. Here we consider a crack coalescence model (CCM) in which two cracks, a larger principal crack and a smaller subsidiary one, exist along the planar fault (Fig. 1a). We presume that frictional strength has been weakened and that any pre-slip has thus occurred on the cracks. Failure in the modelling is described using a slip-weakening friction law originally proposed by Ida (1972). The fault strength τ, once reaching the peak strength τ_p, decreases linearly to the residual strength τ_r with ongoing fault slip D, according to,

$$\tau = \tau_r + (\tau_p - \tau_r)(1 - D/D_c)H(1 - D/D_c), \quad (1)$$

where $H(\cdot)$ and D_c are the Heaviside function and critical slip displacement, respectively. The minimum nucleation size L_c obtained from the fracture energy balance (for Poisson ratio $\nu = 0.25$), as described by Andrews (1976) and Kame *et al.* (2003), is determined using

$$L_c = \frac{16}{3\pi} \frac{\mu G}{(\tau_0 - \tau_r)^2} = \frac{64}{9\pi^2} \left(\frac{\tau_p - \tau_r}{\tau_0 - \tau_r} \right)^2 R_0, \quad (2)$$

where μ is the shear modulus and G is the fracture energy of the medium. Here $R_0 = (3\pi/4)[\mu G/(\tau_p - \tau_r)^2]$ is the approximate slip-weakening zone length at low rupture velocities as derived by Palmer & Rice (1973), which is to be resolved spatially in the following computations. We choose a specific length L of the main crack that is slightly greater than L_c. This produces an initial stress concentration which is slightly larger than the peak strength at both ends of the main crack and which accelerates finite rupture in the first dynamic time steps (Kame *et al.* 2003).

2.2 Elastodynamic boundary integral equation method

We use the elastodynamic boundary integral equation method (BIEM) to simulate spontaneous rupture propagation. Employing the discretized form of the elastodynamic representation theorem, evaluated by Kame & Yamashita (1999a); the following algebraic equation is obtained for the change in shear stress on spatial cell l at the end of time step n due to the slip rate history up to that point in time:

$$\Delta \tau^{ln} = -\frac{\mu}{2C_s} V^{ln} + \sum_{k=0}^{n-1} \sum_i K^{ln:ik} V^{ik}. \quad (3)$$

Here V^{ik} is the slip rate of cell i during time step k and $K^{ln:ik}$ is the response to unit slip rate in cell i in time step k. C_s represents the shear wave speed of the medium. The first term on the right-hand side, $-\mu/2C_s$, is the radiation damping term (Cochard & Madariaga 1994). It represents the instantaneous contribution of the current slip rate to the shear stress at the same position. The second term represents the contribution of the past slip rate history. The total shear stress, which is the sum of the incremental stress and the pre-stress $\tau = \Delta \tau + \sigma_{xy}^0$, is considered in determining the slip rate that meets the slip-weakening friction law (eq. 1) at the current time step. Once the slip rate history over the fault has been obtained, the displacement velocity at an arbitrary point can be synthesized from similar discretized forms (Tada & Madariaga 2001).

All computations are made using the following non-dimensional quantities: length $x^* = x/\Delta s$, time $t^* = C_s t/\Delta s$, stress $\sigma_{ij}^* = \sigma_{ij}/(-\sigma_{yy}^0)$, strength $\tau^* = \tau/(-\sigma_{yy}^0)$, slip $D^* = \mu D/(-\sigma_{yy}^0 \Delta s)$, slip rate $V^* = \mu V/(-\sigma_{yy}^0 C_s)$, displacement acceleration $A^* = \mu \Delta s A/(-\sigma_{yy}^0 C_s^2)$ and frequency $f^* = \Delta s f/C_s$. We base the normalization on the fault normal stress $-\sigma_{yy}^0$ (taking tensile stresses to be positive), the cell size Δs and the shear wave speed C_s. We choose the non-dimensional time interval $\Delta t^* = 0.25$ and the collocation parameter $e_t = 1.0$ to satisfy the BIEM stability condition in mode II (Tada & Madariaga 2001). This enables us to avoid introducing any artificial damping terms for the planar fault calculations. The star symbols are omitted hereafter for brevity.

2.3 Numerical settings and procedure for spontaneous crack growth

To most clearly elucidate the rupture complexity associated with the dynamic coalescence process, the pre-stress state (σ_{xy}^0) and frictional properties $(\tau_p, \tau_r$ and $D_c)$ in CCM are presumed to be uniform on the unbroken parts of the fault. First we set $\sigma_{xy}^0 = 0.24$ and $\tau_r = 0.12$ (Fig. 1b). This means that the stress drop, defined by $\Delta \sigma = \sigma_{xy}^0 - \tau_r$, is also uniformly distributed $(= 0.12)$. We set the peak strength to be $\tau_p = 0.60$ and choose a uniform critical slip distance $D_c = 3.92$ (Fig. 1a), so that the slip-weakening zone length R_0 is finely resolved as $R_0 = 9.6\Delta s$, where Δs is the spatial cell size and $\mu = 1.0$ is arbitrarily chosen in the computations. In fact, our simulations confirm that the dynamic slip-weakening zone lengths are well resolved—they correspond to nine grid intervals just after dynamic propagation and smoothly reduce to three grid intervals as the rupture velocity accelerates, approaching the limit velocity of C_R, the Rayleigh wave speed. The critical length of the main crack is determined by eq. (2) to be $L_c^{main} = 110.7$ and we introduce a larger initial crack length $L^{main} = 120$ on $-240 \le x \le -120$ for dynamic propagation to start from its tips. Another subsidiary crack of assumed length $L^{sub} = 60 (= L^{main}/2)$ is introduced on $60 \le x \le 120$ in the CCM.
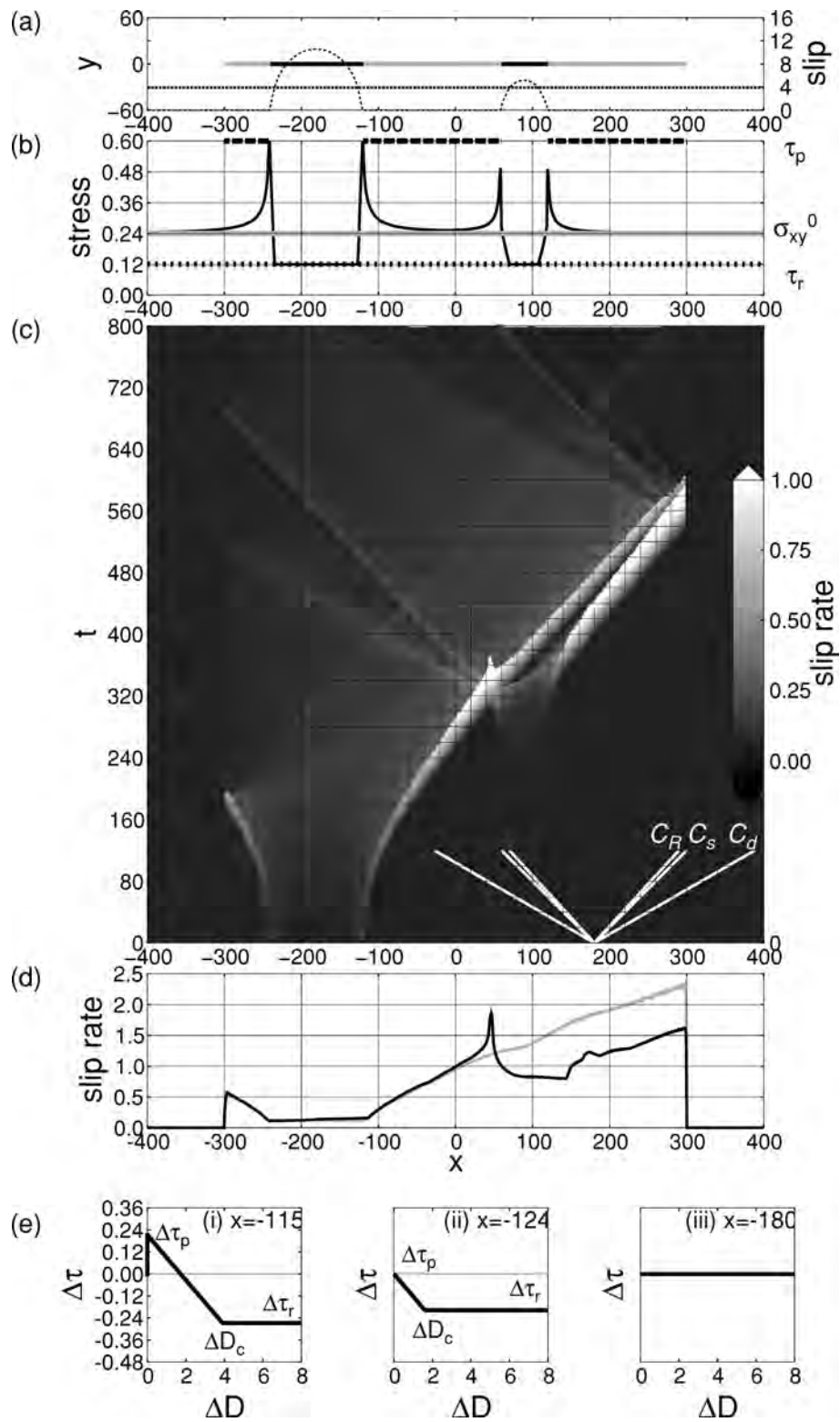
Figure 1. (a) Configuration of the crack coalescence model (CCM) consisting of two pre-existing cracks (solid lines) on a planar fault (a grey line). Thick-dotted and thin-dashed lines indicate the distribution of the critical slip distance D_c and the pre-slip distribution D_0, respectively. (b) Distribution of the peak strength τ_p (thick dashed line), the residual strength τ_r (dotted line) and the pre-stress σ_{xy}^0 (grey line). The solid line indicates the initial stress distribution τ_0 just before dynamic propagation. (c) Spatiotemporal evolution of the simulated slip rate of the CCM. (d) Maximum slip rate experienced at each position. The solid black line represents the CCM and the grey line is for a simple model. (e) Three types of incremental constitutive curves.

Preventing any slip outside these two regions, the pre-slip distribution D_0 in the static equilibrium state is determined. This distribution must satisfy the slip-weakening boundary condition expressed in eq. (1), and the calculation is performed using the elastostatic BIEM (Kame *et al.* 2003). For the pre-slip solution to also exist on the subsidiary crack, we tentatively employ a lower strength of $\tau_p = 0.30$ there. This condition yields a smaller critical length $L_c^{sub} = 15.6$ and the assumed subsidiary crack, being larger than this, is arrested by the higher-strength regions outside it (Fig. 1b). Once we obtain the pre-slip distribution, we can evaluate the initial shear stress distribution $\tau_0 = \Delta\tau + \sigma_{xy}^0$. Having determined the initial state (D_0 and τ_0), dynamic rupture is allowed to propagate along the planar fault. The entire rupture propagation process is arrested by unbreakable barriers $\tau_p = +\infty$ at $x = \pm 300$, that is at both ends of the planar fault.

3 RESULTS

3.1 Dynamic coalescence rupture process in the CCM

Dynamic rupture in the CCM begins at $t = 0.00$. The slip rate at each time step is determined by BIEM, and the resulting slip rate history is shown in Fig. 1(c). The Rayleigh C_R, shear C_s and dilatational C_d wave speeds are plotted for reference. Initially, the main crack propagates bilaterally and the propagation speed smoothly accelerates, approaching C_R. Localized higher slip rates are generated just behind the rupture front and the maximum rates increase with progressive crack growth (Fig. 1d). This tendency is more clearly illustrated by the grey line, which corresponds to a simple model in which the rupture front spreads monotonically without coalescence starting from homogeneous source parameters. In the CCM, the rupture reaches the left barrier at $t = 174.00$, where it is arrested.

Dynamic slip on the subsidiary crack is not excited until the seismic wave reaches it. On arrival, it strengthens the stress concentration at both ends. The left tip stress exceeds the peak strength at $t = 186.75$, when leftward dynamic propagation commences. Dynamic propagation commences at right tip at $t = 272.25$. The approaching crack tips of the main and subsidiary cracks finally coalesce at $x = 45$ and $t = 303.50$. At the point of coalescence, a relatively higher slip rate is excited, whose maximum is about 1.6 times larger than that of the simple model (Fig. 1d). Localized higher slip rates of such values have been commonly observed in previous coalescence simulations and been attributed to stress interaction between the approaching rupture fronts (Yamashita & Umeda 1994; Fukuyama & Madariaga 2000; Dunham *et al.* 2003).

The higher slip rate region does not propagate following dynamic coalescence. Minor disturbances in the slip rate spread bilaterally from the coalescence point at two different speeds of C_d and C_R on the slipping surface. Similar disturbances are generated by the rupture arresting at the barriers. These are interfacial waves, whose allowable propagation speeds are predicted theoretically to be C_d, C_s and C_R in mode II (Yamashita 1983), but C_s phases are hardly identified in our simulations. The disturbances are very small because there is no strain energy release with propagation and the stresses on the slipping region maintain a constant residual value of τ_r. However, a prominent localized higher slip-rate region moves rightwards on the residual stress surface. It originates not from the coalescence but from the propagating rupture front of the main crack. On coalescence, the right rupture front suddenly transfers into the subsidiary right-hand side crack tip, and the higher slip-rate region in the vicinity of the former rupture front is thus left behind. It propagates at a speed of C_R as an interfacial wave. The new rupture front again accelerates to C_R gradually. Accordingly, the two localized higher slip-rate regions, originating from the new and former rupture fronts, propagate simultaneously until they are terminated successively at the $x = +300$ barrier at $t = 537.50$.

3.2 Seismic radiation from dynamic coalescence in CCM

The seismic wavefield in the CCM can now be synthesized and examined with particular attention paid to waves associated with dynamic coalescence. Fig. 2(a) shows snapshots of the wavefield in the fault-parallel (FP) and fault-normal (FN) components. To emphasize the high-frequency radiation, we plot accelerations. For the purposes of these plots, the velocity wavefield is first synthesized using the integral kernels for the displacement velocity derived by Tada & Madariaga (2001), and the finite difference is then taken between successive time steps to obtain acceleration. The time-series is then low-pass filtered to below a non-dimensional frequency 0.10 to reduce spurious high frequencies associated with discrete rupture propagation.

Initially, seismic waves emitted from the bilaterally propagating rupture fronts are identifiable in both the FP and FN components ($t = 160$). Leftward rupture is arrested at $x = -300$, after which a stopping phase spreads cylindrically from the arresting point ($t = 240, 320, \ldots$). The approaching rupture fronts of the two cracks coalesce at $x = 45$, and a distinct 'coalescence phase' is emitted and spreads cylindrically ($t = 320, 400, \ldots$). On the rightward rupture's arrest at $x = +300$, two stopping phases are radiated, corresponding to termination of the two propagating localized higher slip-rate regions, and they propagate cylindrically again ($t = 560, 640, \ldots$). These cylindrical phases, yielded by stopping and coalescence, are clearly identified in both components. In terms of propagation speeds, both the dilatational and shear waves can be identified.

In appearance, the coalescence phase has striking similarities to the stopping one. Both phases spread cylindrically from their points of emission and exhibit the same radiation pattern, namely the far-field four-lobed patterns of the radial and transverse components due to a double couple source (Aki & Richards 2002). For the dilatational waves (the radial radiation component), maxima appear in the 45° and 135° directions, and the node appears in the 90° direction in both components. For the transverse shear waves, the maximum in FP and the node in FN appear in the 90° direction, where the angles are measured counter-clockwise from the x-axis. These similar seismic radiation patterns can be attributed to the similar spatiotemporal slip-rate evolutions (Fig. 1c). With regard to rupture arrest, the propagating localized higher slip-rate regions are discontinuously terminated in space by the barriers at $x = \pm 300$. In the vicinity of the coalescence point, a similar spatial cut-off occurs after coalescence: on the subsidiary crack, little slip-rate is generated due to there being no release of strain energy. These sudden spatial cut-offs against the propagating higher slip-rate regions give rise to the similar seismic radiation patterns.

Seismic radiation associated with the propagating higher slip-rate regions is quite different. The radiated waves prevail along the fault surface in FN and are shear waves in terms of propagation speed. Such waves are commonly referred to as a 'rupture directivity pulse' in observations of historic very large earthquakes and are responsible for the strongest ground motions (Irikura *et al.* 1996; Somerville *et al.* 1997; Somerville 2003). Note that the directivity phases in the FN component continue to propagate beyond the arresting point at $x = +300$, even after the rupture propagation
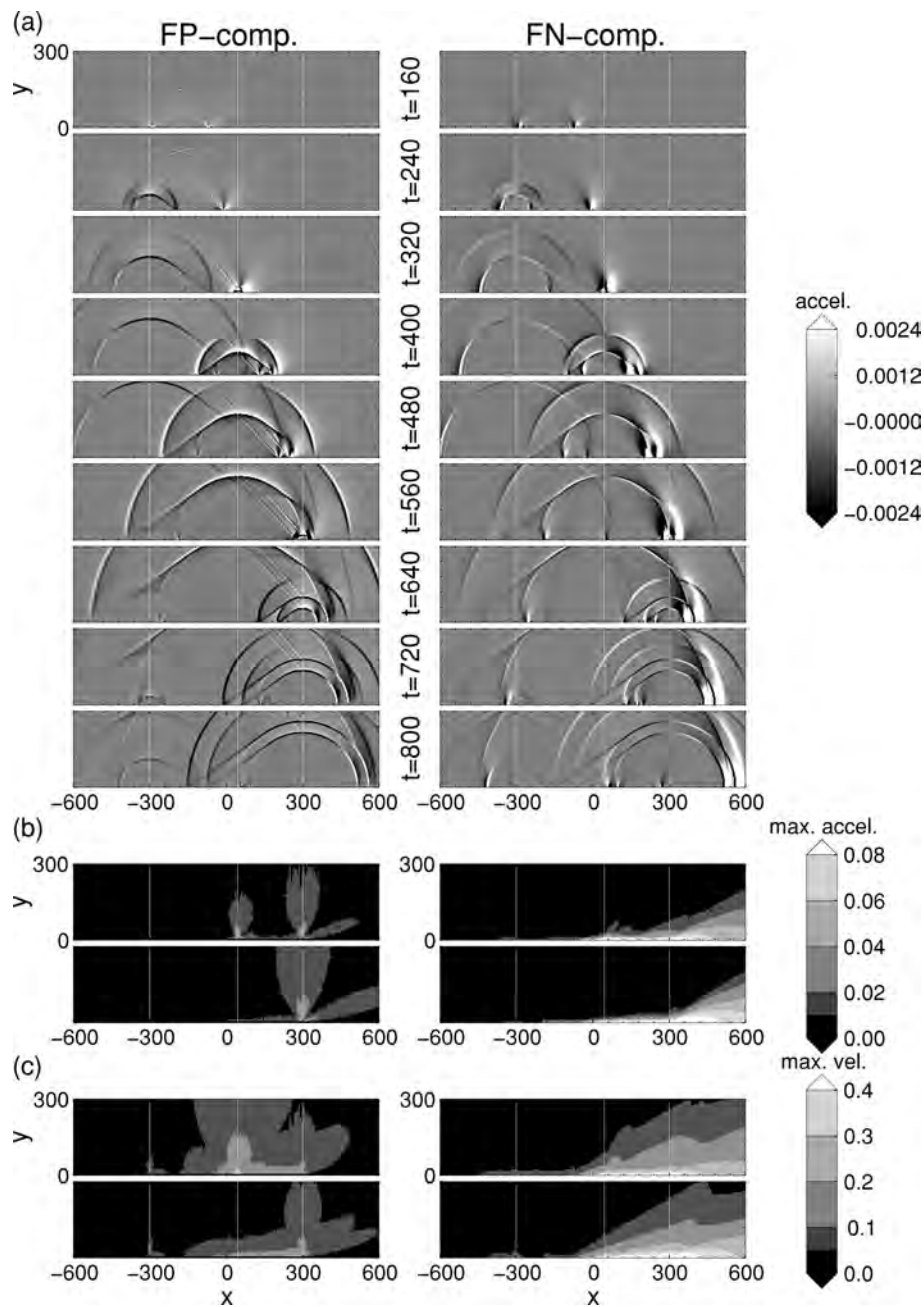
Figure 2. (a) Snapshots of the acceleration wavefield of the CCM. The left and right columns show the fault-parallel (FP) and fault-normal (FN) components, respectively. Based on the final rupture extent of $-300 \leq x \leq 300$ and the model symmetry with respect to the y-axis, each shot is displayed within the region $-600 \leq x \leq 600$ and $0 \leq y \leq 300$. Thin lines indicate the locations of the crack coalescence point ($x = 45$) and barriers ($x = \pm 300$). (b) The maximum acceleration distribution of the CCM (top) and the simple model (bottom). (c) The maximum velocity distribution of the CCM (top) and the simple model (bottom).

terminates there. Waves from the two separate higher slip rate regions are clearly distinguishable from each other after coalescence ($t = 400, 480, \ldots$).

Figs 2(b) and (c) illustrate the maximum distributions of the acceleration and velocity for each component. Note that the velocity waveforms have also been low-pass filtered to below a non-dimensional frequency of 0.10. In each figure, the top and bottom panels correspond to the CCM and the simple model (employed in the preceding subsection), respectively. In the FP component for the CCM (Figs 2b and c top), the coalescence and stopping shear waves play important roles in determining the distinct patterns: the max-

ima are distributed normal to the fault plane, which directly reflects the radiation pattern for the shear waves with a maximum in the 90° direction and their less rapidly decaying cylindrical propagation property. On the other hand, phases associated with the propagating higher slip-rate regions are dominant in the FN component. The maximum contours are densely distributed along the plane and are amplified by the directivity effect in the rupture propagation direction. The bottom panels of Figs 2(b) and (c) illustrate results for the simple model, for reference. In the FP component, we observe larger accelerations and velocities due to the stopping phase around $x = +300$. This is because the maximum slip rate has grown to be
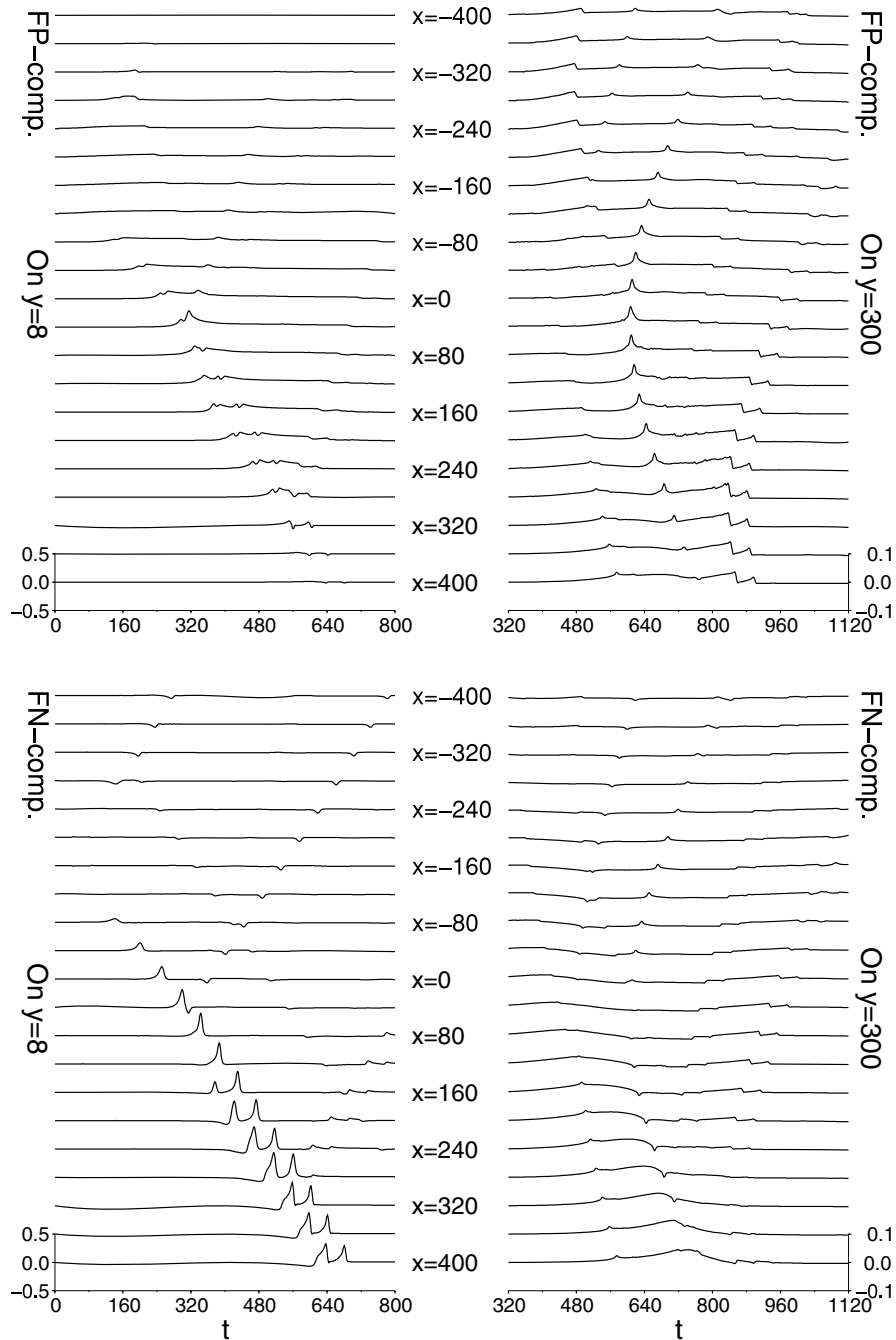
Figure 3. Velocity waveforms observed at stations evenly distributed between $x = -400$ and $+400$ along $y = +8$ (left-hand column) and $y = +300$ (right-hand column). The upper and lower rows correspond to the FP and FN components, respectively.

larger in the simple model than in the CCM just before arresting, as shown in Fig. 1(d). In the FN component, the maxima are also stronger than for the CCM for the same reason. This implies that the strongest ground motion depends on how large the maximum slip rate becomes: the strain energy released in the CCM is not concentrated on a single rupture front but split into two fronts, resulting in the smaller maximum slip rate and the weaker seismic radiation accordingly. In general, the acceleration distributions are steeper than the velocity distributions, due to being relatively enriched in higher-frequency energy.

Fig. 3 shows the velocity waveforms generated by the CCM. The observation points are aligned on the two lines parallel to the fault plane: one lies at $y = +8$, very close to the fault, and the other is at $y = +300$, a half-length of the final rupture length away from the plane. The stations are put on each line at intervals of 40 between $x = -400$ and $+400$. Along $y = +8$, the first arrivals of the coalescence phase, $(x, t) = (40, 300)$, and the stopping phases from the both ends of the fault, $(x, t) = (-320, 170)$ and $(320, 560)$, can be identified in the FP records. On the other hand, phases from the propagating localized higher slip rate regions are dominant in the FN component. Due to the low attenuation there, this is directly reflected in the near-field radiation pattern of each phase in each component. Note that the waveforms in the FN component ($x \geq 160$) clearly show two successive pulses, corresponding to the two

split higher slip rate regions. Along $y = +300$, the propagating higher slip-rate phases have markedly decayed, and only the cylindrical phases can be identified in both components. The shear wave arrivals of the coalescence phase, $(x, t) = (40, 600)$, and the stopping phases from both ends of the fault, $(-320, 460)$ and $(+320, 840)$, are clearly identified for the FP records. On the FN component, the earlier-arriving dilatational waves of those phases have amplitudes comparable to the shear waves. These velocity waveforms also exhibit distinct differences in the radiation and propagation properties between the cylindrical phases and the propagating higher slip-rate phases. With respect to the terminology used to describe seismic radiation from a double couple point source (Aki & Richards 2002), the near-field term seems to prevail for the propagating higher slip-rate phase and the far-field term for the cylindrical one. As illustrated by Fig. 2(a), a quadratic pattern is again recognized for the far-field radiation of the two cylindrical phases observed along $y = +300$. For the transverse shear waves, the maxima in the FP component and the nodes in the FN component are in the $90°$ direction. Likewise, for the dilatational waves, the maxima appear in the $45°$ and $135°$ directions and the node appears in the $90°$ direction.

3.3 Reconstruction of a seismically comparable single crack model (SCM) and apparent heterogeneity in the source parameters

Another goal of this paper is to examine what heterogeneous source parameters will be inferred for a dynamic coalescence process if the assumption of a 'monotonically spreading rupture front' is made in the waveform inversion analysis. Such an assumption is not valid for in a CCM and thus some apparent heterogeneity will necessarily emerge in the inversion results, which we examine further here.

To characterize such heterogeneity in the CCM, we attempt to reconstruct a seismically comparable single crack model (SCM). In a SCM, the rupture fronts spread monotonically for heterogeneous source parameters and no dynamic coalescence occurs. 'Seismically comparable' here is taken to mean that the SCM radiates seismic waves comparable to those of CCM. Because the rupture front assumption holds throughout rupture growth in a SCM, the reconstructed source parameters contain apparent heterogeneity that would be inferred from the inversion of a CCM event. In the following, we consider two models for the reconstruction: as neither of them used alone can reproduce the CCM results completely, we employ a certain quantifiable validation to evaluate the two alternatives in terms of waveform fitting to the CCM results.

We first summarize briefly a standard procedure for the reconstruction of dynamic source parameters, based on a kinematic waveform inversion analysis (Ide & Takeo 1997). This approach usually consists of the following three steps. (1) The slip rate history is first determined by an inversion assuming that the rupture front spreads monotonically. (2) The stress change history on the fault is next calculated by solving the elastodynamic equation of motion for a given displacement boundary condition, namely the slip rate history computed in the previous step. (3) Finally, by combining the two histories, the constitutive relation between the slip and stress changes is determined on the fault surface, from which the dynamic parameters can be derived.

Our reconstruction of a SCM starts from step (2), that is, assuming that the slip rate history in the CCM is specified completely. This is justified if we eventually succeed in the reconstruction of SCM, whose slip rate can be ideally inferred from the inversion even if the assumption of a monotonically spreading rupture front is

given. Note that the given slip rate history itself tells us neither the initial stress distribution τ_0 nor the pre-slip distribution D_0 shown in Figs 1(a) and (b)—only changes from these are measurable. When the slip rate history has been given, the incremental stress history $\Delta\tau^{ln}$ on each element is determined by the elastodynamic BIEM (eq. 3). The incremental slip history ΔD^{ln} is determined by time step summation of the given slip rate multiplied by Δt, ultimately yielding the incremental constitutive relationship between $\Delta\tau^{ln}$ and ΔD^{ln} for each element.

We next proceed to step (3). Fig. 1(e) shows three types of the incremental constitutive curves. In type (i), the incremental stress initially increases to the peak value $\Delta\tau_p$ and then decreases with incremental slip ΔD. After the slip has reached the incremental critical displacement ΔD_c, the stress maintains a residual level of $\Delta\tau_r$. This behaviour pertains to the unbroken part of the fault in the CCM ($D_0 = 0$). In type (ii), the stress simply decreases with slip and ΔD_c becomes shorter than the original D_c. This pertains to the pre-slip part where $D_0 < D_c$ in the CCM. In type (iii), the stress remains unchanged and this corresponds to the pre-slip region where $D_0 > D_c$. Conventionally, $\Delta\tau_p$ and the negative of $\Delta\tau_r$ are referred to as the strength excess and the stress drop ($\Delta\sigma = -\Delta\tau_r$), respectively, in the terminology of dynamic source parameters (Quin 1990).

Fig. 4(a) shows the distribution of the dynamic source parameters $\Delta\tau_p$, $\Delta\tau_r$ and ΔD_c extracted from each curve and compiled over the fault. It can be noted immediately that they are represented by the subtraction of the initial state from the original slip-weakening friction law (eq. 1) as:

$$\Delta\tau = \Delta\tau_r + (\Delta\tau_p - \Delta\tau_r) \times (1 - \Delta D/\Delta D_c)H(1 - \Delta D/\Delta D_c),$$
(4)

where $\Delta\tau_p = (\tau_p - \tau_0) \times [1 - H(D_0)]$, $\Delta\tau_r = (\tau_r - \tau_0)$ and $\Delta D_c = (D_c - D_0) \times H(D_c - D_0)$. Note that if we simulate spontaneous rupture obeying eq. (4), without any constraints on the rupture fronts (that is, dynamic slip is potentially allowed at any time at all points on the fault), the CCM slip rate is perfectly reproduced. In that case, the dynamic slip starts from a zero-strength region ($-240 \leq x \leq -120$), and then another zero-strength region ($60 \leq x \leq 120$) is dynamically excited by stress wave interaction, before the rupture front of the first slipping region arrives. Accordingly, the dynamic coalescence between two slipping regions does occur— this is not what is to be reconstructed.

To achieve a 'monotonically spreading rupture front', we have to impose the constraint that each point on the fault outside the first zero-strength region is allowed to slip dynamically only after the rupture fronts has reached it. A dynamic rupture model with this constraint is the first candidate for the SCM we seek: we refer to this model as SCM1 and simulate its spontaneous rupture growth. As a preliminary check on the SCM reconstruction, we compare the maximum slip rate distributions for the CCM and SCM1, because they affect the resultant waveforms significantly (Fig. 4b). It is clear that SCM1 does not match the CCM adequately: the peak of SCM1 is shifted from $x = 45$, the dynamic coalescence point to $x = 59$, the original subsidiary crack tip in the CCM and the maximum level stays lower on $x \geq 150$. This is because the stress interaction with the dynamically excited slip on the second zero-strength region prior to coalescence is lost in SCM1. Fig. 4(c) show comparisons of the CCM and SCM1 in two representative velocity waveforms. One is for the cylindrical coalescence and stopping phases, and the other is for the propagating higher slip rate phases. They are observed at $(x, y) = (0, 300)$ in the FP component and at $(x, y) = (320, 8)$ for the FN component, respectively. Their waveforms do not fit each other
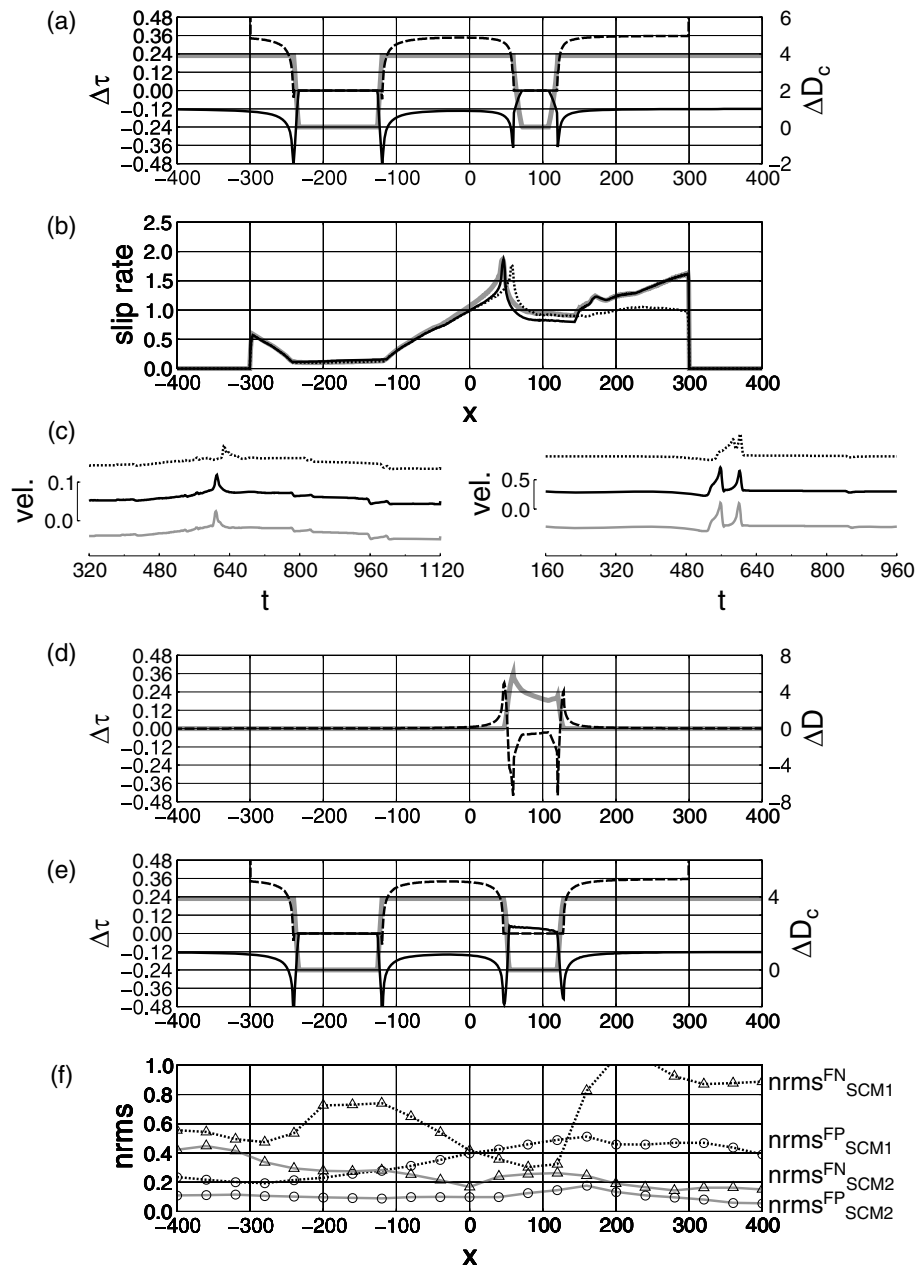
Figure 4. (a) Distribution of the incremental constitutive parameters: strength excess $\Delta\tau_p$ (dashed line), critical displacement ΔD_c (grey line) and residual strength $\Delta\tau_r$ (solid line). The stress drop $\Delta\sigma$ is the negative of the residual strength ($= -\Delta\tau_r$). These parameters are hereafter employed for SCM1 with the constraint of a monotonically spreading rupture front. (b) The maximum slip rate distribution for three models: CCM (solid line), SCM1 (dotted line) and SCM2 (grey line). (c) The velocity waveforms of the three models observed at $(x, y) = (0, 300)$ for the FP component (left-hand side) and at $(x, y) = (320, 8)$ for the FN component (right-hand side). The notations are the same as in (c). (d) Distribution of the slip increment $\Delta D^{\text{excited}}$ (grey line) and the stress increment $\Delta\tau^{\text{excited}}$ (dashed line) on the subsidiary crack. (e) Distribution of dynamic source parameters of SCM2 with modification of the increments $\Delta D^{\text{excited}}$ and $\Delta\tau^{\text{excited}}$. The notations are the same as in (b). (f) Normalized root mean square (nrms) values of the waveform misfit function calculated at each observation station. Circles are for the FP component on $y = 300$ and triangles are for the FN component on $y = 8$. Dotted and grey lines represent SCM1 and SCM2, respectively.

very well, as anticipated on the basis of the misfit in the maximum slip-rate distributions.

To improve on SCM1, we must take into account the stress interaction with the dynamically excited slip on the subsidiary crack. The contribution of this dynamic stress is extracted as follows: first, we draw a line in Fig. 1(c) starting from the coalescence point $(x, t) = (45, 303.50)$ and increasing with a slope of C_d. Dynamically excited slip prior to this line can be regarded as what happened be-

fore dynamic coalescence in terms of causality. Fig. 4(d) shows the resultant slip increment $\Delta D^{\text{excited}}$: it is distributed on $46 \leq x \leq 127$ and becomes larger than originally, because of the dynamic propagation before coalescence. The stress increment $\Delta\tau^{\text{excited}}$ due to $\Delta D^{\text{excited}}$ is calculated using the elastostatic BIEM (Fig. 4d). These increments of slip and stress are then included in the source parameters of SCM1 ($\Delta\tau_p$, $\Delta\tau_r$ and ΔD_c) as follows: $\Delta\tau_p^{\text{SCM2}} = (\Delta\tau_p - \Delta\tau^{\text{excited}}) \times [1 - H(\Delta D^{\text{excited}})]$, $\Delta\tau_r^{\text{SCM2}} = (\Delta\tau_r - $

$\Delta\tau^{\text{excited}}$), $\Delta D_c^{\text{SCM2}} = (\Delta D_c - \Delta D^{\text{excited}}) \times H(\Delta D_c - \Delta D^{\text{excited}})$. These modified values constitute SCM2 (Fig. 4e), with which the constraint of a 'monotonically spreading rupture front' and spontaneous rupture propagation is then simulated. Note that the total coseismic slip in SCM2 is less than in the CCM due to the subtracted slip component, $\Delta D^{\text{excited}}$. The maximum slip rate and waveforms are shown in Figs 4(b) and (c) and SCM2 seems to represent a substantial improvement over SCM1.

As a quantifiable validation of the improvement of SCM2 in the waveform fitting to the CCM, we employ the normalized root mean square (nrms) of the velocity waveform misfit function. The definition of nrms used here is

$$\text{nrms} = \sum_k \left(\dot{U}_{\text{SCM(i)}}^k - \dot{U}_{\text{CCM}}^k\right)^2 / \sum_k \left(\dot{U}_{\text{CCM}}^k\right)^2, \quad (i = 1, 2), \quad (5)$$

where $\dot{U}^k$ represents a synthesized velocity at $t = k\Delta t$, $(k = 1, \ldots, 4800)$ for each model. For example, in Fig. 4(c) the values are $\text{nrms}_{\text{SCM1}}^{\text{FP}} = 0.40$ and $\text{nrms}_{\text{SCM2}}^{\text{FP}} = 0.10$ (left-hand side) and $\text{nrms}_{\text{SCM1}}^{\text{FN}} = 0.86$ and $\text{nrms}_{\text{SCM2}}^{\text{FN}} = 0.16$ (right-hand side). We calculate nrms values for the waveforms observed along $y = 300$ for the FP component and $y = 8$ for the FN component, to focus on the cylindrical phases and the propagating higher slip rate phases, respectively. Fig. 4(f) shows the nrms value at each station. These results confirm quantitatively that SCM2 yields improved waveform fittings: the averages are $\text{nrms}_{\text{SCM1}}^{\text{FP}} = 0.39$ and $\text{nrms}_{\text{SCM2}}^{\text{FP}} = 0.12$ on $y = 300$, and $\text{nrms}_{\text{SCM1}}^{\text{FN}} = 0.66$ and $\text{nrms}_{\text{SCM2}}^{\text{FN}} = 0.25$ on $y = 8$, respectively. Accordingly, SCM2 is regarded as the preferred plausible model in the reconstruction of the SCM. Note that nrms is relatively close between SCM1 and SCM2 at a range of $-400 \leq x \leq -240$ in both components: the discrepancy in the coalescence phases is less significant there because of their relatively smaller amplitudes compared with the dominating almost identical stopping phases from the left barrier.

We further examine the heterogeneous source parameters appearing in SCM2. Dynamic nucleation starts from the two points ($x = -241, -119$) where the strength excess $\Delta\tau_p$ is negative and the stress drop $\Delta\sigma(= -\Delta\tau_r)$ is largest. As the rupture front spreads, $\Delta\tau_p$ increases and $\Delta\sigma$ decreases rapidly. This directly reflects the initial state of the CCM as incrementally shown in eq. (4) (Fig. 4a) and is responsible for the gradual initial acceleration of propagation speed. At the arresting points $x = \pm 300$, $\Delta\tau_p$ is estimated as the maximum stress experienced in the CCM. As to heterogeneity associated with dynamic coalescence, $\Delta\tau_p$ and $\Delta\sigma$ change at the same rate towards the coalescence point. Note that this part does not exist there originally but is dynamically constructed due to the moving subsidiary crack tip in the CCM. At the coalescence point $x = 45$, $\Delta\sigma$ has a sharp peak due to the square-root singularity of the crack tip (precisely speaking, the singularity is weakened in a slip-weakening model), and this generates the localized higher slip rate. Across this point, $\Delta\sigma$ abruptly decreases to negative values, and this suppresses the slip rate to values near zero there. This results in a spatial cut-off of the higher slip rate region. Across $x = 125$, a singularity-like increase in the stress drop increases the slip rate, but the accompanying discontinuous increase in $\Delta\tau_p$ suppresses acceleration of the propagation speed.

Overall, we observe with SCM2 a singularity-like increase in the stress drop and a sudden decrease in the strength excess at the coalescence point of the CCM. This feature does not exist originally but is constructed dynamically. The heterogeneity appearing in SCM2 can approximately account for the waveforms of the CCM: it is an alternative quantitative representation of the somewhat qualitative explanation of 'the rupture front interaction' in the previous coalescence simulations.

4 DISCUSSION

4.1 High-frequency radiation mechanism of dynamic coalescence

High-frequency radiation from earthquakes has been a major concern in engineering seismology circles. Here we discuss the mechanism by which high-frequency waves are generated due to dynamic coalescence based on our simulation results.

The stopping phase has long been known as the strongest source of high-frequency radiation, which has the minimum ω^{-2} decay at high frequencies in the displacement spectrum. Madariaga (1976) showed numerically that radiation of ω^{-2} type occurs due to rupture arrest in a 3-D circular expanding crack model. Madariaga (1977) also demonstrated analytically for a 2-D problem that ω^{-2} radiation is generated by the rupture speed discontinuity—stopping. As shown by our 2-D calculations, the sudden arrest of rupture by a barrier results in a spatial cut-off in the slip rate evolution. It temporally induces a sharply negative change in the increasing moment release rate for the spreading rupture, which is an essential factor in the overall ω^{-2} high-frequency radiation mechanism. In addition, Madariaga (1983) analytically demonstrated that the arresting of a rupture results in a step-type wave-front velocity radiation. In our simulations, such stopping phase characteristics are clearly seen in the waveforms for both the CCM and the simple model at $(x, y) = (0, 300)$ in the FP component (Fig. 5a). They both contain step-like changes at $t = 420, 600$ corresponding to the dilatational and shear waves of a stopping phase propagating from the left barrier at $x = -300$. Feature associated with a second stopping phase from the right barrier at $x = 300$ are also identified at $t = 860$ and 1040 in the simple model and at $t = 780$ and 960 in the CCM. The waveforms in the simple model, not possessing the coalescence phase, actually reveal ω^{-1} high-frequency decay in the velocity spectrum, or equivalently ω^{-2} high-frequency radiation of the stopping phases in the displacement spectrum (Fig. 5b).

With respect to the dynamic coalescence process in the CCM, the propagating slip-pulse is also spatially cut-off across the coalescence point as shown in Fig. 1(c). It necessarily results in a similar abrupt change in the moment release rate, and the same ω^{-2} characteristics in the displacement spectrum is also expected at high-frequencies. In addition, we have noted that the dynamic coalescence process involves another high-frequency radiation factor: the generation of localized higher slip rates due to coalescence. We have demonstrated that this could be equivalently generated by a singular stress drop in the SCM2 model. It is demonstrated theoretically by the analysis of a propagating mode III crack with a certain constant propagation speed that the strong ω^{-2} wave is also radiated by a square-root singularity in the stress drop (Madariaga 1983). SCM2 does contain such a stress-drop singularity. This means that dynamic coalescence involves two ω^{-2} radiation mechanisms operating simultaneously and is therefore more efficient in radiating high-frequency waves than stopping phases. The SCM2 waveforms actually show ω^{-1} high-frequency decay in the velocity spectrum (or equivalently ω^{-2} high-frequency decay in the displacement spectrum), at levels higher than in the simple model (Fig. 5b). This is because of the predominant amplitude of the coalescence phase at about $t = 620$ in the CCM (Fig. 5a). Note that the effects of strength excess have less significance in generating ω^{-2} radiation, unless the change is large enough to cause a discontinuous change
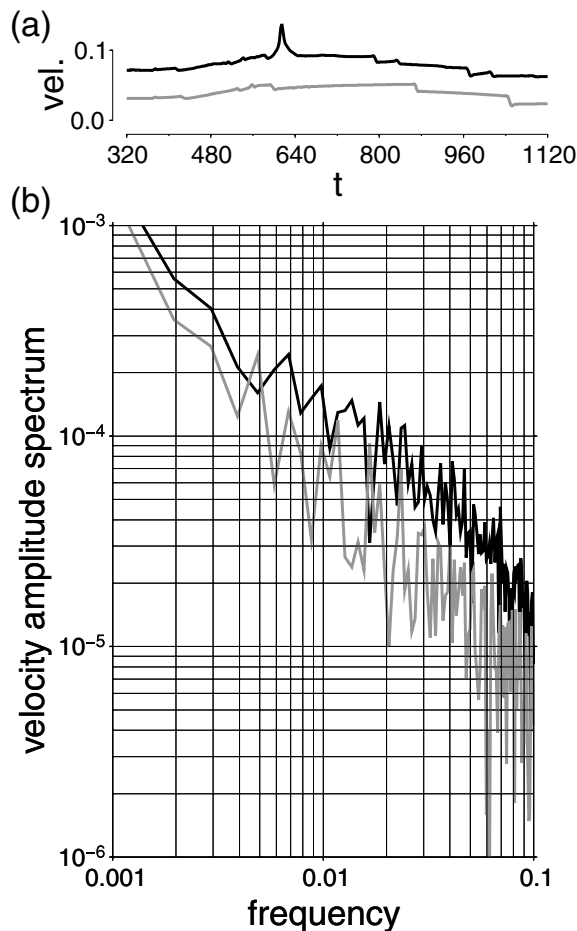
Figure 5. (a) Velocity waveforms of the CCM (solid line) and the simple model (grey line) for the FP component observed at $(x, y) = (0, 300)$. (b) Velocity amplitude spectra for the two models. The Fourier transform is done in the time range $160 \le t \le 1184$.

in the propagation speed, as quantitatively shown by Madariaga (1983); this does not occur in our simulation. In SCM2, there are three other stress-drop singularities ($x = -241, -119$ and 125) and the same ω^{-2} high-frequency radiation is expected from them: they are known as starting phases (Madariaga 1977). The starting phases from $x = -241$ and -119 can be identified in Fig. 2(a) ($t = 160, 240$). Their very small amplitudes can be attributed to the accompanying increasing strength excess regions at each point of emission (Fig. 4e): this suppresses rupture growth and brings about very small initial moment release rates (Fig. 1c).

4.2 Limitations of the reconstruction and the possibility of determining coalescence heterogeneity

We have analysed the CCM and reconstructed a seismically comparable SCM, with heterogeneity equivalent to dynamic coalescence. However, we have employed an *ad hoc* method in the reconstruction and not actually performed a true inversion analysis. Here we discuss the limitations of our method and the possibility of finding coalescence heterogeneity via formal inversion.

We have simulated dynamic crack coalescence for only one configuration and considered a relatively small subsidiary crack. This is because the reconstruction of the SCM is limited to cases in which the dynamically excited slip rate before coalescence can be omitted

in seismic radiation. If this condition is not met, the reconstruction of the SCM fails because the seismic radiation before the rupture front arrival cannot be accounted for. An example is the approaching rupture fronts for two growing cracks with the same dimension. Clearly, the dynamic coalescence is not represented by a single crack growth model in this case. However, the high-frequency radiation mechanism of dynamic coalescence, which originates from higher slip rate generation and the spatial cut-off in the slip rate evolution, remains valid for any coalescence cases.

Regarding the possibility of accurately observing coalescence heterogeneity, most waveform data have insufficient resolution to determine the exact rupture front evolution, as referred to in the introduction. Based on the shortest reliable wavelengths, a whole fault is usually divided into at best a few tens of elements along the fault trace. On the other hand, dynamic modelling requires much finer meshes to represent faithfully a continuously propagating rupture front. Here we have employed 600 elements along the fault and found that for the specific coalescence heterogeneity, singularity-like increases appeared in the stress drop and the strength excess at scales shorter than 20 elements. This is not large enough to resolve in the actual inversions and any sharp singularities would typically be averaged within a coarse inversion mesh. Accordingly, there may be practical difficulties in detecting heterogeneity responsible for dynamic coalescence in waveform inversions.

5 CONCLUSIONS

We have considered a crack coalescence model (CCM) in which the dynamic coalescence of two mode II cracks occur on a planar fault. We first simulated spontaneous rupture growth in this CCM using BIEM and investigated the complexity in the resultant slip rate history. We have shown that localized higher slip rates are generated by dynamic coalescence as a result of stress interaction between approaching crack tips, even for homogeneous source parameters. We then synthesized the seismic radiation in the CCM and found striking similarities in the radiation and propagation properties between coalescence and stopping phases. Both phases are radiated from a spatial cut-off in the slip rate evolution, for which ω^{-2} high-frequency radiation is anticipated, and spread cylindrically to dominate acceleration and velocity distributions in the FP component. The strongest ground motion is, however, generated by the propagating higher slip-rate phases with its rupture directivity effect on the FN component. We finally reconstructed a seismically comparable single crack model (SCM) to examine the apparent inhomogeneity that would have been inferred from waveform inversion analysis. In the SCM, we observe a singularity increase in the stress drop distribution at the coalescence point in the CCM, which is an additional factor in the production of ω^{-2} radiation from dynamic coalescence. These results imply that the coalescence process is more efficient in radiating ω^{-2} waves than stopping phases.

As noted in the introduction, the apparent heterogeneity on a planar fault could also come from non-planar fault structures, such as kinks, steps, bends and branches. Their seismic radiation characteristics and equivalent source parameters are fascinating problems for future research. This class of studies needs to be further advanced to obtain deeper understanding of dynamic earthquake process and seismic radiation mechanisms.

ACKNOWLEDGMENTS

MEXT, Japan and the Earthquake Research Institute cooperative research program.

REFERENCES

Adda-Bedia, M. & Madariaga, R., 2008. Seismic radiation from a kink on an antiplane fault, *Bull. seism. Soc. Am.,* in press.

Aki, K. & Richards, P.G., 2002. *Quantitative Seismology*, 2nd edn, University Science Books, Sausalito.

Ando, R., Kame, N. & Yamashita, T., 2007. An efficient boundary integral equation method applicable to the analysis of non-planar fault dynamics, *Earth Planets Space, 59,* 363–373.

Andrews, D.J., 1976. Rupture velocity of plane strain shear cracks, *J. geophys. Res., 81,* 5679–5687.

Aochi, H. & Fukuyama, E., 2002. Three-dimensional non-planar simulation of the 1992 Landers earthquake, *J. geophys. Res., 107*(B2), doi:10.1029/2000JB000061.

Bhat, H.S., Dmowska, R., Rice, J.R. & Kame, N., 2004. Dynamic slip transfer from the Denali to Totschunda faults, Alaska: testing theory for fault branching, *Bull. seism. Soc. Am., 94*(6B), 202–213.

Chatterjee, A.K. & Knopoff, L., 1990. Crack breakout dynamics, *Bull. seism. Soc. Am., 80,* 1571–1579.

Cochard, A. & Madariaga, R., 1994. Dynamic faulting under rate-dependent friction, *Pageoph, 142,* 419–445.

Das, S. & Aki, K., 1977. Fault plane with barriers: a versatile earthquake model, *J. geophys. Res., 82,* 5658–5670.

Dunham, E.M., Favreau, P. & Carlson, J.M., 2003. A supershear transition mechanism for cracks, *Science, 299,* 1557–1559.

Fukuyama, E. & Madariaga, R., 2000. Dynamic propagation and interaction of a rupture front on a planar fault, *Pageoph, 157,* 1959–1979.

Harris, R. & Day, S.M., 1993. Dynamics of fault interaction: parallel strike-slip faults, *J. geophys. Res., 98,* 4461–4472.

Ida Y., 1972. Cohesive force across the tip of longitudial-shear crack propagation, *J. geophys. Res., 77,* 3796–3805.

Ide, S. & Takeo, M., 1997. Determination of constitutive relations of fault slip based on seismic wave analysis, *J. geophys. Res., 102,* 27 379–27 391.

Irikura, K., Iwata, T., Sekiguchi, H., Pitarka, A. & Kamae, K., 1996. Lesson from the 1995 Hyogo-ken Nanbu earthquake: why were such destructive motions generated to buildings?, *J. Nat. Disas. Sci., 18,* 99–127.

Kame, N. & Yamashita, T., 1997. Dynamic nucleation process of shallow earthquake faulting in a fault zone, *Geophys. J. Int., 128,* 204–216.

Kame, N. & Yamashita, T., 1999a. Simulation of the spontaneous growth of a dynamic crack without constraints on the crack tip path, *Geophys. J. Int., 139,* 345–358.

Kame, N. & Yamashita, T., 1999b. A new light on arresting mechanism of dynamic earthquake faulting, *Geophys. Res. Lett., 26,* 1997–2000.

Kame, N. & Yamashita, T., 2003. Dynamic branching, arresting of rupture and the seismic wave radiation in a self-chosen crack path modelling, *Geophys. J. Int., 155,* 1042–1050.

Kame, N., Rice, J.R. & Dmowska, R., 2003. Effects of pre-stress state and rupture velocity on dynamic fault branching, *J. geophys. Res., 108*(B5), 2265, doi:10.1029/2002JB002189.

Kame, N., Saito, S. & Oguni, K., 2008. Quasi-static analysis of strike fault growth in layered media, *Geophys. J. Int., 173,* doi:10.1111/j.1365-246X.2008.03728.x.

Kostrov, B.V. & Das, S., 1988. *Principles of Earthquake Source Mechanics*, pp. 171–258, Cambridge University Press, Cambridge.

Madariaga, R., 1976. Dynamics of an expanding circular fault, *Bull. seism. Soc. Am., 65,* 163–182.

Madariaga, R., 1977. High-frequency radiation from crack (stress drop) models of earthquake faulting, *Geophys. J. R. astr. Soc., 51,* 625–651.

Madariaga, R., 1983. High-frequency radiation from dynamic earthquake fault models, *Annales Geophysicae, 1,* 17–23.

Madariaga, R., Ampuero, J.P. & Adda-Bedia, 2006. Seismic radiation from simple models of earthquakes, in *Earthquakes: radiated Energy and the Physics of Faulting*, pp. 223–236, eds Abercrombie, R., McGarr, A., Kanamori, H. & DiToro, G., American Geophysical Union, Washington.

Palmer, A.C. & Rice, J.R., 1973. The growth of slip surfaces in the progressive failure of over-consolidated clay, *Proc. R. Soc. London A, 332,* 527–548.

Quin, H., 1990. Dynamic stress drop and rupture dynamics of the October 15, 1979 Imperial Valley, California, earthquake, *Tectonophysics, 175,* 93–117.

Somerville, P.G., 2003. Magnitude scaling of the near fault rupture directivity pulse, *Phys. Earth planet. Inter., 137,* 201–212.

Somerville, P.G., Smith, N.F., Graves, R.W. & Abrahamson, N.A., 1997. Modification of empirical strong ground motion attenuation relations to include the amplitude and duration effects of rupture directivity, *Seism. Res. Lett., 68,* 199–222.

Tada, T. & Madariaga, R., 2001. Dynamic modelling of the flat 2-D crack by a semi-analytic BIEM scheme, *Int. J. Numer. Mech. Eng., 50,* 227–251.

Umeda, Y., Yamashita, T., Tada, T. & Kame, N., 1996. Possible mechanisms of dynamic nucleation and arresting mechanisms, *Tectonophysics, 261,* 179–192.

Yamashita, T., 1983. High-frequency acceleration radiated by unsteadily propagating cracks and its near-source geometrical attenuation, *J. Phys. Earth, 31,* 1–32.

Yamashita, T. & Umeda, Y., 1994. Earthquake rupture complexity due to dynamic nucleation and interaction of subsidiary faults, *Pageoph, 143,* 89–116.